

CrossMark
click for updatesCite this: *J. Mater. Chem. A*, 2014, 2, 13602

Exposed facets induced enhanced acetone selective sensing property of nanostructured tungsten oxide†

Qian-qian Jia, Hui-ming Ji,* Da-hao Wang, Xue Bai, Xiao-hong Sun and Zheng-guo Jin

WO₃ nanorods with exposed (100) and (002) facets were fabricated *via* a hydrothermal route using different directing agents. Microspheres that were assembled randomly by WO₃ nanorods with exposed (002) facets were porous with a specific surface area of 62.2 m² g⁻¹. Acetone gas sensing properties of the as-prepared sensors were investigated for the breath diagnosis of diabetes. The acetone detection limit of WO₃ microspheres was 0.25 ppm, and the response (R_a/R_g) to 1 ppm acetone was 3.53 operated at 230 °C with a response and recovery time of 9 and 14 s, respectively. WO₃ samples with exposed (002) facets exhibited better acetone sensitivity and selectivity than those with (100) facets. The sensing mechanism was discussed in detail. Because of the asymmetric distribution of unsaturated coordinated O atoms in the O-terminated (002) facets, the surface had an extent of polarization. Induced local electric dipole moment contributed to easy adsorption and reaction between the (002) facets and acetone molecules with a large dipole moment at low working temperatures. Room temperature PL spectra clearly displayed that the WO₃ samples exposed with (002) facets had numerous oxygen vacancies and defects, resulting in excellent acetone sensing properties.

Received 18th April 2014
Accepted 23rd June 2014

DOI: 10.1039/c4ta01930j

www.rsc.org/MaterialsA

Introduction

Among the hundreds of volatile organic compounds (VOCs) in human breath, acetone is a biomarker of type-1 diabetes.¹ The average concentration of acetone in healthy human breath is lower than 0.8 ppm, while in a diabetic patient it is higher than 1.8 ppm.^{2,3} The accurate and rapid detection of low concentrations of acetone is necessary for exhaled breath sensors based on gas sensing materials. Tungsten oxide (WO₃) is widely studied because of its feasible fabrication, low cost, and excellent gas sensing properties towards different oxidizing and reducing gases.^{4–6} Acetone is a kind of reducing gas decreasing the resistance of WO₃ after being induced into air. The chemical reactions between the disturbing gases (such as ethanol, ammonia, benzene and methanol) and the materials surface are similar with those of acetone. To achieve accurate disease diagnosis, the selectivity of the sensing material is essential but difficult to realize.

Monoclinic II (ϵ -WO₃) phase is ferroelectric with a large electric dipole moment but it is only stable at -40 °C. Acetone

has a large dipole moment and can react selectively with ϵ -WO₃. WO₃ nanoparticles with a ϵ -WO₃ phase could be obtained by doping with Cr and Si *via* a flame spray pyrolysis method.^{7,8} However, strict operation condition increases fabrication difficulty, and it is still difficult to ensure their thermal stability. The selective acetone sensing property could also be enhanced by fabricating Pt-functionalized WO₃ hemitube networks.⁹ However, noble metal modification increases the fabricating cost, and the catalyst effect of noble metal nanoparticles is only good for their sensitivity. Hierarchical WO₃ nanostructures can facilitate gas diffusion and provide efficient electron transport because of their large surface-to-volume ratio.^{10–13} Gas sensitivity can be improved in this manner but it has a little effect on the acetone sensing selectivity.

Surface properties such as catalytic, adsorption, and gas sensing are strongly dependent on the exposed planes for single crystal materials. In recent years, several studies on metal oxide nanocrystals with predominantly highly reactive surfaces have been reported. Co₃O₄ nanosheets with exposed {112} planes displayed better catalytic activity than nanocrystals with {001} and {011} planes.¹⁴ The high-index {332} facets of SnO₂ had the most dangling bonds, showing selective sensing performance to ethanol.^{15,16} ZnO with exposed active polar (0001) facets exhibited significantly higher catalytic activity, better photocatalytic performance, and excellent gas sensing properties.^{17–20} WO₃ nanorods grown along [110] with exposed (001) facets exhibited higher adsorption capacity for organic dyes than

Key Laboratory of Advanced Ceramics and Machining Technology of Ministry of Education, School of Materials Science and Engineering, Tianjin University, Tianjin 300072, China. E-mail: jihuuming@tju.edu.cn; Tel: +86-022-27890485

† Electronic supplementary information (ESI) available: SEM and XRD analysis of WO₃ nano-materials after heat-treatment, dynamic response curves of gas sensors, and the 1 ppm acetone selective properties. See DOI: 10.1039/c4ta01930j

those along the [001] axis with (100) facets.²¹ Octahedral WO₃ showed good sensing properties to benzene gas, which might be due to its exposed (111) facets;²² however, the sensing mechanism was not clear. Numerous attempts have been reported with respect to controlling the exposure of certain facets to improve the gas sensing properties of ZnO and SnO₂ but reports on the surface design and control of WO₃ for gas sensing applications are still lacking.²³ Based on the density functional theory (DFT) calculations, WO₃ (001) facets could effectively detect NO₂ gas,²⁴ and the O-terminated (001) surface of hexagonal WO₃ was more active to react with CO molecules than the WO-terminated (001) surface.²⁵ Therefore, it is possible to achieve better acetone gas sensing sensitivity and selectivity by the fabrication of certain crystal facets exposed WO₃ nano-materials.

In this work, WO₃ samples exposed with different facets were prepared *via* a hydrothermal method, and their gas sensing performance was measured. It was shown that WO₃ nanorods with exposed (002) facets exhibited excellent acetone sensing selectivity against ethanol and other reducing gases. The microspheres assembled by WO₃ nanorods with exposed (002) facets had the largest specific surface area, thereby the highest gas sensitivity. This result was considered to be originated from the asymmetric distribution of unsaturated coordinated O atoms in the O-terminated (002) facets and their abundant oxygen vacancies and structural defects. To the best of our knowledge, the controllable exposure of the crystal facets of WO₃ and their effect on gas sensitivity and selectivity are reported for the first time.

Experimental

Synthesis of materials

The fabricated WO₃ nanorods grown along the [001], [110] axis, and microspheres assembled by nanorods along [110] were named as NR-1, NR-2, and MS, respectively. The typical preparation procedure of NR-1 is as follows: 1.320 g Na₂WO₄·2H₂O was weighed and dissolved in 40 mL of deionized H₂O. pH was adjusted to 2.0 by the dropwise addition of dilute H₂SO₄ under constant magnetic stirring at room temperature. Light yellow H₂WO₄ was precipitated gradually. Then, the solution was added with 4.0 g Na₂SO₄ and 1.008 g oxalic acid as the directing agent. The precursor solution was transferred into a Teflon-lined 50 mL autoclave for hydrothermal reaction at 180 °C for 24 h. After cooling to room temperature, the prepared WO₃ powders were centrifuged and washed alternately with distilled water and ethanol several times. Finally, the obtained products

were dried in air at 80 °C for 4 h. According to the raw materials and hydrothermal conditions listed in Table 1, NR-2 and MS samples were also prepared.

Characterization

The morphological features of WO₃ were investigated by field emission scanning electron microscopy (SEM, Hitachi, S4800), energy dispersive spectrometry (EDS), transmission electron microscopy, and high-resolution transmission electron microscopy (TEM, HR-TEM, FEI Tecnai G2 F20). The crystalline structures of the products were examined by X-ray diffraction (XRD) *via* a Rigaku D/max 2500 diffractometer at 40 kV and 200 mA with Cu K α radiation ($\lambda = 0.15406$ nm) ranging from 10° to 70°. The photoluminescence (PL) spectra of WO₃ were recorded at room temperature using a spectrometer (Jobin Yvon Fluorolog 3-21, Jobin Yvon Inc.) at an excitation wavelength of 325 nm.

Gas sensing characterization

Side-heating gas sensors were prepared to measure the gas sensing properties of the WO₃ samples. Fig. 1a shows the photograph and schematic diagram of a typical gas sensor. An appropriate amount of WO₃ powders were mixed with several drops of distilled water to form a paste, which was then coated onto an alumina tube whose length and diameter were 4 and 1.2 mm, respectively. Electric contacts were made with a pair of Au electrodes and four Pt wires. A Ni-Cr alloy filament used as a heater was inserted into the tube. The temperature of the coated tube was controlled by regulating the current from 0 to 300 mA. The gas sensors were placed in a gas chamber (20 L). Fig. 1b shows the measurement of the electric circuit of gas sensing properties. In the test process, a heating voltage (V_h) and test voltage (V_t) were supplied to the sensor. A load resistor was connected to the sensor, whose voltage (V_L) and resistance (R_L) were measured and used for calculating and outputting the corresponding sensor resistance through a computer connected to the testing apparatus. The gas sensors were aged completely for several hours at their working temperature before measurement to improve their mechanism strength and electric contact. The gas sensing properties were measured by a CGS-8 intelligent gas sensing analysis system (Beijing Elite Tech. Co. Ltd., China). A given amount of target gases were injected into the closed gas chamber by a microliter syringe and mixed with a fan for several minutes. After each measurement, the sensors were exposed to atmospheric air by opening the chamber. The sensor response (S) to the target gas was defined as:

Table 1 Raw materials and treating conditions of NR-1, NR-2, and MS^a

Sample	Tungsten source	Acid source	pH	Capping agent	Hydrothermal condition
NR-1	Na ₂ WO ₄ ·2H ₂ O	H ₂ SO ₄	2.0	Na ₂ SO ₄ and oxalic acid	180 °C 24 h
NR-2	Na ₂ WO ₄ ·2H ₂ O	H ₂ SO ₄	1.0	(NH ₄) ₂ SO ₄ and oxalic acid	180 °C 10 h
MS	(NH ₄) ₁₀ W ₁₂ O ₄₁ ·xH ₂ O	H ₂ SO ₄	1.0	(NH ₄) ₂ SO ₄ and oxalic acid	180 °C 10 h

^a All chemical reagents were of analytical grade and obtained from Tianjin Chemical Reagent Factory and Sinopharm Chemical Reagent Co. Ltd. China.

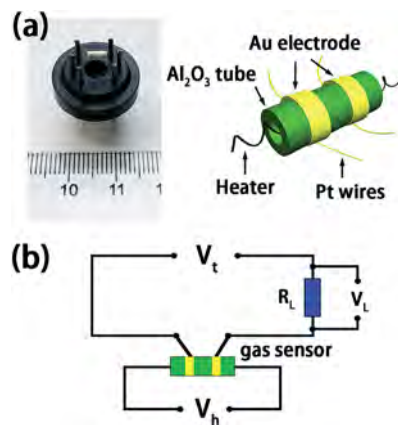


Fig. 1 (a) Photograph and the schematic diagram of a typical gas sensor and (b) the measurement of the electric circuit of gas sensing properties.

$$S = R_a/R_g \quad (1)$$

where R_a and R_g were sensor resistance in air and in a target reducing gas, respectively. The time required to reach 90% variation in resistance upon different gases were defined as the response time and recovery time, respectively. It has been proven by our previous work that the relative humidity has little effect on gas sensing properties²⁶ so the relative humidity (RH) was maintained at approximately 25%, and the ambient temperature was 20 °C.

Results and discussion

Material characteristics

Fig. 2 shows (a1, b1, c1) the SEM images (insets are the sketch maps), (a2, b2, c2) magnified SEM and TEM images, and (a3, b3, c3) HRTEM images (insets are the corresponding FFT images) of NR-1, NR-2, and MS, respectively. The nanorod bundles of NR-1 are in a diameter range of 300–500 nm, which are compactly arranged in parallel by thin nanorods of 10–20 nm. The plane distance along the axis of the WO_3 nanorods of NR-1 is 0.382 nm, revealing that the single crystals were grown along the [001] axis. The NR-2 sample displays well-dispersed nanorods with a diameter of 15–50 nm. The plane distance along the growth direction of NR-2 is 0.368 nm, indicating that the preferred growth direction is [110]. The microspheres of the MS sample have a diameter of 2–3 μm , which are randomly assembled by numerous nanorods of 10–20 nm size. The lattice distance of nanorods from MS is 0.366 nm, indicating a [110] growth direction. It is observed from the FFT images that the three samples are well grown single crystals. The EDS analysis of MS shown in Fig. 2d reveals that WO_3 microspheres are primarily composed of O and W elements. The C element is possibly derived from the remaining oxalate ions during preparation. Pt element is sprayed on the surface for good electric conduction during SEM characterization. The atom ratio of O–W is 2.87, which is smaller than 3, indicating that the fabricated WO_3 microspheres are non-stoichiometric compounds due to the absence of oxygen in the crystal lattice.

The XRD patterns of the NR-1, NR-2, and MS samples and the standard patterns of PDF card nos. 75-2187 and 85-2460 are displayed in Fig. 3a. All the typical diffraction peaks are well-indexed to the profile of hexagonal WO_3 . The (100) peak of NR-1, (002) peaks of NR-2 and MS are significantly stronger than those of the standard patterns. The relative texture coefficient of a certain crystal facet (TC_{hkl}) is defined to evaluate the degree of the crystal facet exposure. The texture coefficients of (100) and (002) facets are given by:^{27,28}

$$\text{TC}_{100} = \frac{I_{100}/I_{100}^0}{I_{001}/I_{001}^0 + I_{100}/I_{100}^0} \quad (2)$$

$$\text{TC}_{002} = \frac{I_{002}/I_{002}^0}{I_{002}/I_{002}^0 + I_{100}/I_{100}^0} \quad (3)$$

Here, TC_{100} and TC_{002} are the relative texture coefficients of the diffraction peaks of (100) over (001), and (002) over (100), respectively. I_{hkl} is the measured diffraction intensity of the (hkl) facet, and I_{hkl}^0 is the corresponding value of the standard XRD patterns measured from the randomly oriented powders. The texture coefficient of h- WO_3 with random crystallographic orientations is 0.5. Fig. 3b displays the texture coefficients of NR-1, NR-2, and MS. As calculated by eqn (2) and (3), TC_{100} of NR-1 is 0.611, TC_{002} of NR-2 and MS are 0.617 and 0.637, respectively. It can be concluded that NR-1 is mainly exposed with (100) facets, while NR-2 and MS are predominantly exposed with (002) facets. This result is in agreement with the HRTEM analysis and the previous report by J. Zhu.²¹ In most cases with inorganic salts as capping agents (NaCl , Na_2SO_4 , K_2SO_4 , *et al.*), hydrothermally synthesized WO_3 nanorods are along the intrinsic c -axis because the surface energy of the (001) crystal facets are higher than the (110) facets. However, the NH_4^+ ions could adsorb on the (001) surface and force WO_3 nanorods to grow along the [110] direction with exposed (001) facets, which are seldom prepared.²¹ Hence, in this experiment, WO_3 nanorods of the NR-1 sample grow along the [001] axis with exposed (100) facets because of Na^+ ions as the capping agent, while the nanorods in NR-2 and MS samples are along the [110] direction with exposed (002) facets because of the existence of NH_4^+ . NH_4^+ ion concentration in the precursor solution for the preparation of MS was higher than that for preparing NR-2, therefore, MS exposes a larger proportion of (002) facets.

Considering the requirement of maintaining the morphology and the structure of the WO_3 samples under a high working temperature, the as-prepared WO_3 powders of NR-1, NR-2, and MS were heat-treated at 300 °C for 0.5 h at a heating rate of 3 °C min^{-1} . It is observed in the SEM images of the three samples (Fig. S1 in the ESI[†]) that the morphologies are almost unchanged after the heat treatment. The XRD patterns and TC_{hkl} of the three samples (Fig. S2 in the ESI[†]) could further display the preservation of the crystal phase structure and their predominant exposed facets of the three samples. The large decrease of the TC_{001} of NR-1 originated from the shrinkage and the damage of the end face of the WO_3 nanorod bundles, which did not occur in the NR-2 and MS samples.

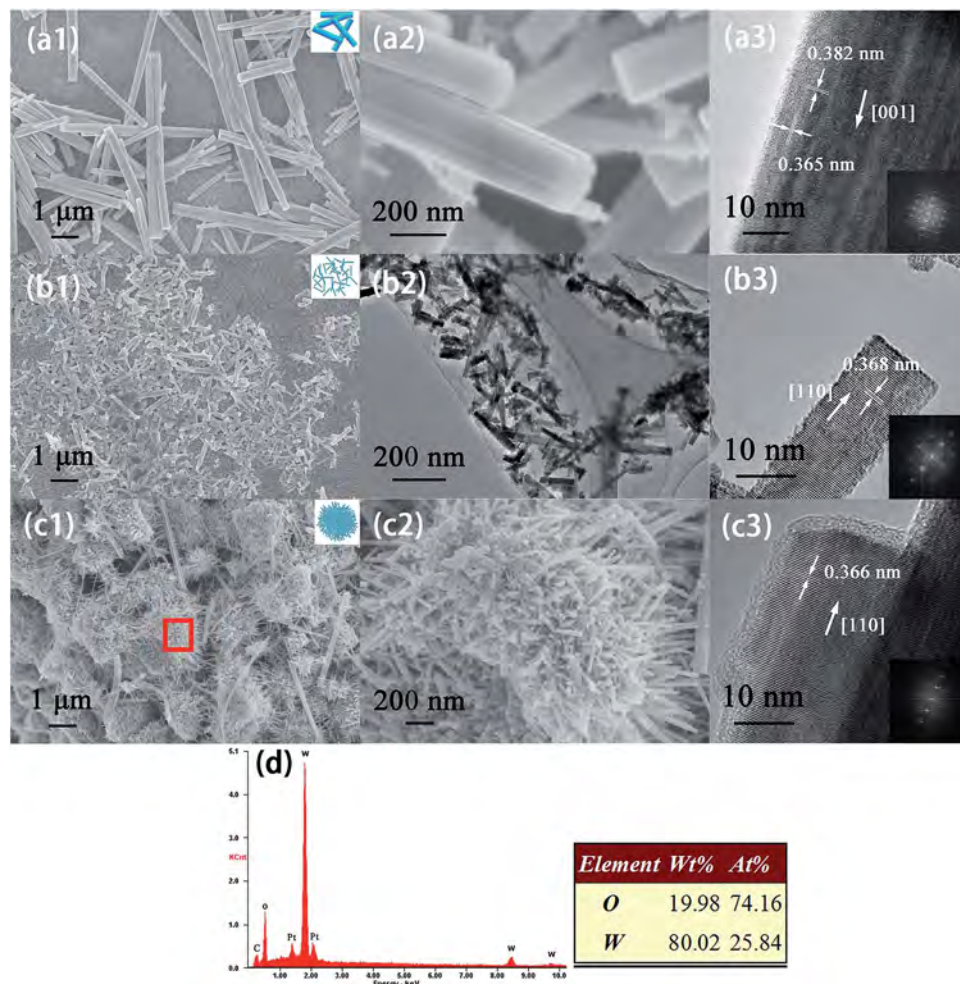


Fig. 2 SEM, TEM, and HRTEM images of the WO_3 samples of (a) NR-1, (b) NR-2, and (c) MS; (d) EDS analysis of MS. (The inset images of a1, b1, and c1 are the sketch maps of the three samples. The inset images of a3, b3, and c3 are the FFT images of the three samples).

Complete nitrogen adsorption–desorption isotherms were measured to gain information regarding the specific surface area (S_{BET}) and pore size distribution of NR-1, NR-2, and MS, as shown in Fig. 4. The S_{BET} of NR-1, NR-2, and MS were evaluated to be 28.6, 32.2, and 62.2 $\text{m}^2 \text{g}^{-1}$, respectively, from data points in the nitrogen adsorption–desorption isotherms using the Brunauer–Emmett–Teller (BET) equation. According to the IUPAC classification,²⁹ the three samples show type II curves with H3 hysteresis loops, indicating that the WO_3 nanostructures are non-porous or macroporous materials. Pore size distribution peaks (inset in Fig. 3) were determined using the Barrett–Joyner–Halenda (BJH) method using the desorption branch of the isotherm. The pore size distribution are not well concentrated for NR-1 and NR-2 but most of the pores are centered at 1.5, 4.4, and 16.9 nm for NR-1, NR-2, and MS, respectively, corresponding to the average gaps between the WO_3 nanorods for the three samples. Apparently, samples with larger S_{BET} and moderate pore sizes are likely to exhibit better gas sensing properties. In the gas sensing process, gas molecules can diffuse into the inside of pores and deplete the surface of nanorods to a large extent.³⁰ The formation of pores in the

three samples was attributed to their assembly mechanism during the hydrothermal reaction. Currently, the shape-controlled assembly mechanism of hierarchical WO_3 nanostructures is still unclear.³¹ However, it is believed that the inherent growth of crystals as well as the specific interaction between the inorganic salt ions and their crystal surfaces might have played a crucial role in controlling the morphology of the final crystals.³¹

Gas sensing properties

The operating temperature of a gas sensor is an important indicator, which is closely related to energy consumption, easy usage, testing convenience, *etc.* During the gas sensing of a semiconductor based gas sensor under thermal activation, the adsorption, surface chemical reaction, and molecules desorption process of the gas molecules will constitute a balance, which exhibits the best response value at optimum operating temperature. In this study, the responses of WO_3 samples towards 30 ppm acetone and ethanol as a function of operating temperature are displayed in Fig. 5. It is depicted that the response value increases first with increasing operating

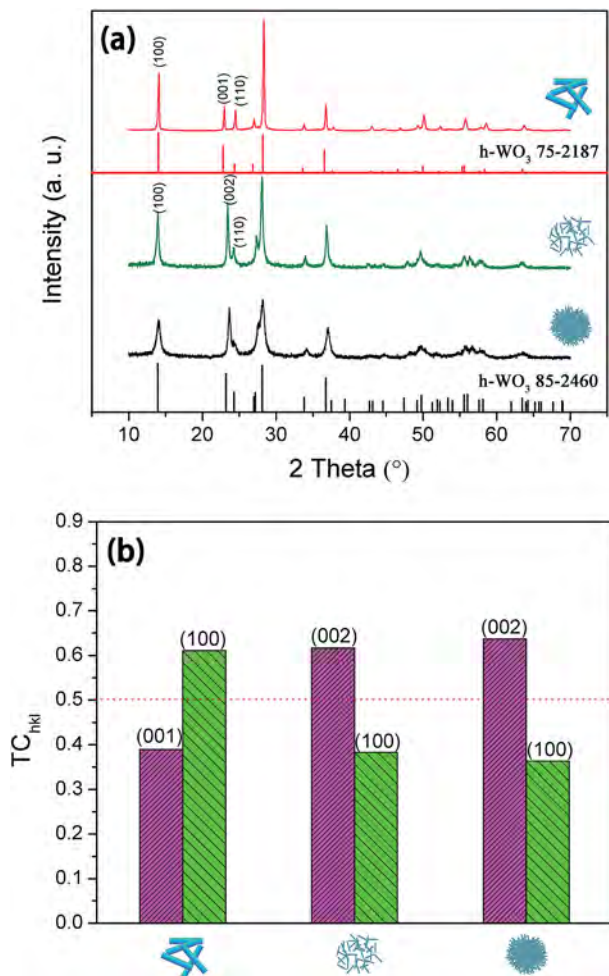


Fig. 3 (a) XRD patterns of NR-1, NR-2, and MS, and the standard patterns of h-WO₃ (PDF card no. 75-2187 and 85-2460) and (b) TC_{hkl} of NR-1, NR-2, and MS.

temperature and then decreases. The maximum responses of NR-1, NR-2, and MS toward 30 ppm acetone are 5.8, 9.1, and 15.4 at an optimum operating temperature of 310, 280, and 230 °C, respectively. Whereas, the responses of NR-1, NR-2, and MS toward 30 ppm ethanol are 6.7, 5.5, and 5.22, respectively, at the same optimum operating temperature of 280 °C. It is observed that the response value toward acetone increases from NR-1 to MS, which might be a result of the increased specific surface area and the increased exposure degree of active (002) facets in the NR-2 and MS samples. At the same time, the optimum operating temperature of NR-1, NR-2, and MS for detecting acetone significantly decreases from 310, 280, to 230 °C, indicating easier adsorption, chemical reaction, and desorption behaviour between gas molecules and the surface of the NR-2 and MS samples. On the other hand, NR-1 exhibits a better response to ethanol than acetone at a lower optimum operating temperature (Fig. 5a). However, NR-2 and MS samples with predominantly exposed (002) facets selectively respond to acetone (Fig. 5b and c), and the selective sensitivity is clearly higher for MS because of the larger exposure of (002) facets.

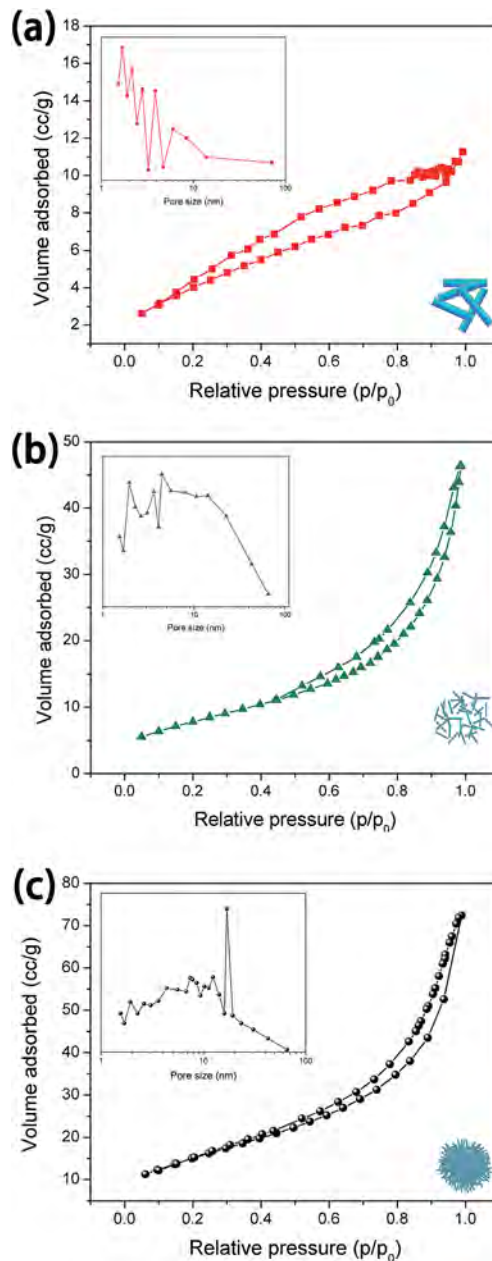


Fig. 4 Nitrogen adsorption-desorption isotherms and pore distribution curves according to the BJH model calculated by the desorption branch of (a) NR-1, (b) NR-2, and (c) MS.

As is well-known, large specific surface area (S_{BET}) can contribute to gas sensitivity but not theoretically benefit acetone selectivity. In this work, the S_{BET} of NR-2 (32.2 m² g⁻¹) is not significantly larger than that of NR-1 (28.6 m² g⁻¹) but the response of NR-2 to acetone increases and to ethanol decreases, leading to remarkable acetone selectivity. For MS, acetone selectivity against ethanol is further enhanced. This acetone gas selectivity performance can possibly originate from the predominantly exposed active (002) facets of NR-2 and MS. Acetone selectivity constitutes an important and practical property for a gas sensor applied in the breath diagnosis of diabetes.

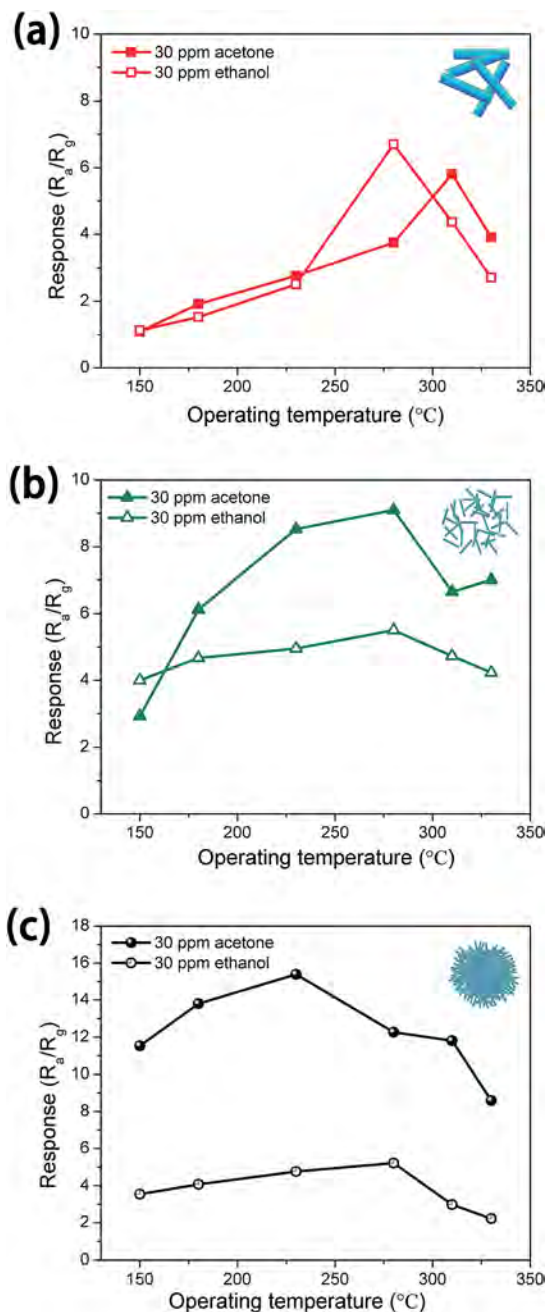


Fig. 5 Responses of (a) NR-1, (b) NR-2, and (c) MS to 30 ppm acetone and ethanol at different operating temperatures.

The responses of NR-2 and MS towards acetone at concentration ranging from 0.5 ppm to 3 ppm are measured at 230 °C (the weak response curve of NR-1 is not shown here). It can be seen from the sensing transient curves (Fig. 6a) that the resistance of the two samples decreases immediately after acetone is induced, exhibiting n-type semiconductor characteristic. The decrease in the resistance of MS is larger than that of NR-2, displaying better acetone sensitivity for MS. The larger initial electric resistance of MS is a result of its high contact barrier height derived from its unique hierarchical nanostructure. The baselines drift slightly due to the unstable surface of single

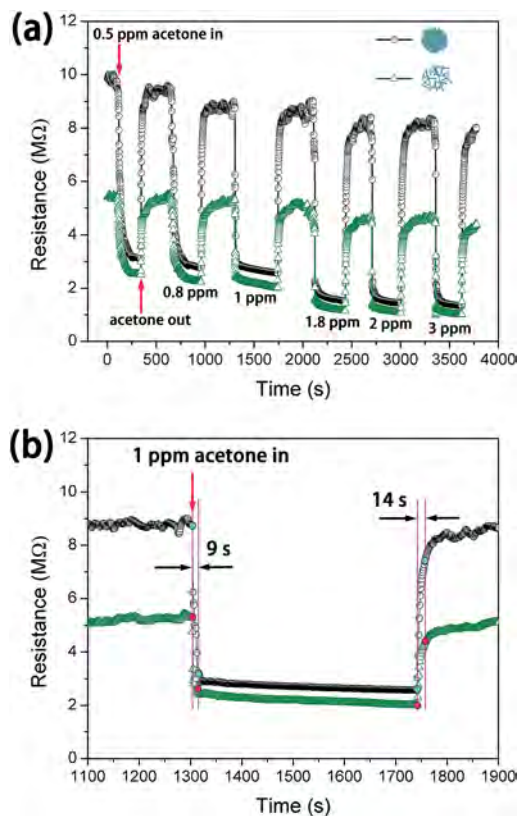


Fig. 6 (a) Sensing transient curve of NR-2 and MS to different concentrations of acetone measured at 230 °C and (b) response and recovery time of NR-2 and MS to 1 ppm acetone.

crystal surfaces but they are still stable enough to enable the practically repeatable detection of low concentrations of acetone. It is clearly observed in the dynamic response curves shown in Fig. S3 in the ESI that the response value of the MS sample increases with an increase in acetone concentration,[†] and that MS is more sensitive than NR-2. The response and recovery time of NR-2 and MS to 1 ppm acetone are 9 and 14 s, respectively, as shown in Fig. 6b.

The sensor responses (S) of the three samples towards various acetone concentrations are calculated and shown in Fig. 7a. Compared with NR-1, NR-2 and MS exhibit better gas sensitivity to acetone. For the MS sample, the response increases from 3.1 to 6.17 as acetone concentration ranges from 0.5 to 3 ppm, which is an evidence for the (002) facets exposed WO_3 microspheres to be a promising candidate in the human breath analysis of type-1 diabetes. On the other hand, the gas responses of NR-2 and MS to ethanol concentration of 0.5 to 3 ppm are lower than 2, indicating that NR-2 and MS exhibit enhanced selective response towards acetone against ethanol gas. The response of various WO_3 nanostructures for the selective sensing of low concentrations of acetone in previous literature and the present study are summarized in Table 2. It is clear from the table that the operating temperature of MS is the lowest among these materials, and the response of MS to acetone is the highest compared with other reported WO_3 sensors. Moreover, the synthesis method of MS is a simple

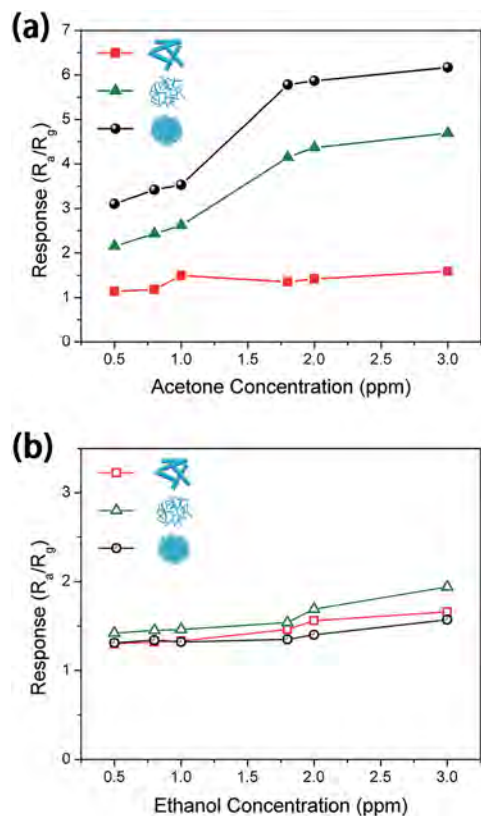


Fig. 7 Responses of NR-1, NR-2, and MS to the different concentrations of (a) acetone and (b) ethanol, measured separately at 230 °C and 280 °C.

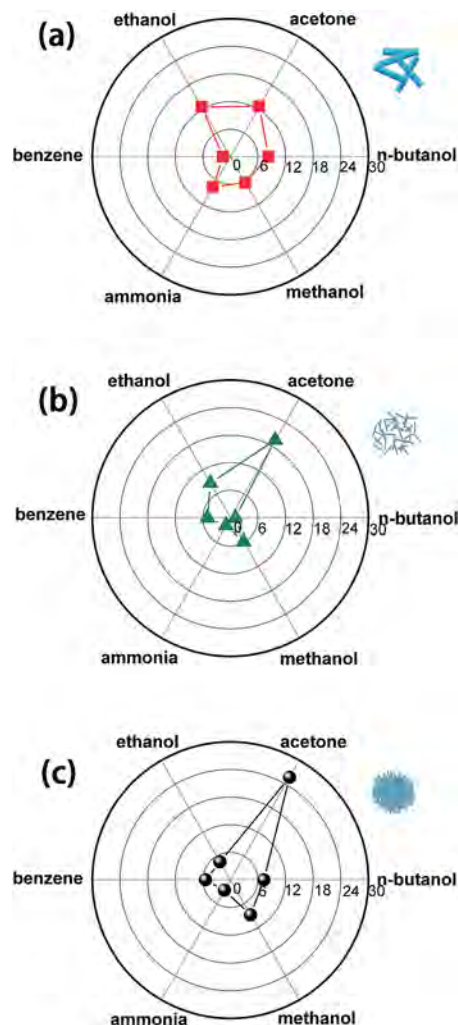


Fig. 8 Response of NR-1, NR-2, and MS to 100 ppm of different reducing gases operated at 230 °C.

hydrothermal method without any ion dopants, while some other WO_3 based nano-materials are fabricated using complicated methods such as flame spray pyrolysis and RF-sputtering.

To further investigate gas selectivity, the responses of NR-1, NR-2, and MS to 100 ppm of various reducing gases (acetone, ethanol, benzene, ammonia, methanol, and *n*-butanol) were measured at 230 °C, and are shown as polar plots in Fig. 8. The gas response to acetone increases from NR-1 to MS, while the response to ethanol decreases. The responses of the three samples towards other reducing gases are negligible. It is concluded that NR-1 exhibits poor acetone gas selectivity and cannot distinguish between acetone and ethanol gas. NR-2 and MS with exposed (002) facets exhibited good selectivity for detecting acetone against other disturbing gases. The response

of MS to acetone and ethanol are 25.71 and 4.5, respectively. In the ppm-region comparison, the sensors exhibit nearly no response to 1 ppm of other gases (benzene, ammonia, methanol, and *n*-butanol), and the response of the three samples to 1 ppm of acetone and ethanol (Fig. S4 in the ESI[†]) also displays excellent acetone selectivity of NR-2 and MS samples with predominantly exposed (002) facets. This result demonstrates that the selective and accurate detection of

Table 2 Gas responses to acetone in the present study and those reported in the literature

Sensing materials	Operating temperature (°C)	Acetone concentration (ppm)	Response (<i>S</i>)	Reference
MS sample	230	0.25	1.47	This study
MS sample	230	0.5	3.1	This study
MS sample	230	1	3.53	This study
Si- WO_3 nanoparticle	400	0.6	2.3	7
Cr- WO_3 nanoparticle	400	1	3.0	8
Pt- WO_3 hemitubes	300	1	2.8	9
Pt- WO_3 nanofiber	350	0.3	1.27	32
WO_3 - Cr_2O_3 thin film	320	1	1.5	33

acetone is successfully realized by controlling the crystal surface of WO_3 without any special doping agent and additional technological treatment.

Gas sensing mechanism

The gas sensing mechanism of n-type semiconductor is based on conductivity changes caused by the adsorption and desorption of gas molecules on the surface.³⁴ Therefore, the gas sensing response of semiconducting materials is strongly related to their surface state. As mentioned above, small crystal size and large specific surface area are definitely advantageous to improve gas sensing response. Moreover, the design and control of the surface state is another possible way to obtain good gas sensitivity and selectivity.

In the present study, the NR-1 sample has (100) facets exposed, while NR-2 and MS are predominantly exposed with (002) facets. Fig. 9 depicts the geometrical structures of the (100) facet of h- WO_3 (PDF card no. 75-2187) and the (002) facet of h- WO_3 (PDF card no. 85-2460), following the coordinate data of W and O atoms from the corresponding standard ICSD patterns. The respective facets are represented by dashed lines. It is clearly noticeable that in the single unit cell, there are two 4-coordinated W atoms and one 2-coordinated O atom in the WO-terminated (100) facet (Fig. 9a). In contrast, the O-terminated (002) facet contains five 1-coordinated O atoms (marked with purple color for clear observation), as shown in Fig. 9b. As reported by the DFT method,²⁵ the O-terminated (001) surface is more active than a WO-terminated (001) surface. Therefore, gas molecules are more likely to adsorb on the (002) facets containing unsaturated coordinated O atoms as chemical adsorption, leaving more oxygen vacancies and resulting in a larger charge transfer from gas molecules to the materials

surface. This is the main reason for WO_3 nanorods with largely (002) facets exhibiting better gas sensing response.

Furthermore, the arrangement of atoms in the (100) facet is symmetric as observed in the top view picture (Fig. 9c). While in the (002) facet of h- WO_3 (PDF card no. 85-2460), O atoms are displaced off from the center of the crystal face and edge. This asymmetric arrangement is possibly caused by the distortion of $[\text{WO}_6]$ octahedra, which is familiar in the metastable WO_3 phase structures. These acentric O atoms can cause the non-uniform distribution of electron cloud around the (002) facet, leading to local electric polarization to some extent. The dipole moment of acetone (2.88 D) is significantly larger than other gases;³⁵ thus, the interaction between acetone molecules and the (002) facet of h- WO_3 is considerably stronger, displaying the observed significant selectivity. Moreover, easier chemical adsorption and reaction results in lower operating temperature for samples with exposed (002) facets.

The intrinsic sensing characteristics of WO_3 samples are analysed using room temperature photoluminescence (PL) measurements to investigate the native structural defects of the WO_3 nanostructures. As clearly shown in Fig. 10a, when the samples are excited at 325 nm, the luminescence peak intensity order is: MS > NR-2 > NR-1. After peak separation using the Gaussian fit method, the PL spectra of the WO_3 samples are divided into several individual peaks, as shown in Fig. 10b–d. The peaks centered at ca. 374 nm in the UV emission region originate from intrinsic band to band transition emission.³⁶ Lee *et al.* also reported a similar PL peak at a wavelength of 350 nm for tungsten oxide. In our study, the intrinsic emission peaks are red-shifted compared with other reports,^{37,38} implying a reduced band gap in the present tungsten oxide nanorods, which is attributed to the quantum-confinement-effect in these nanostructures.^{39,40} Another strong-intensity region is the blue emission peaks centered at ca. 435, 465, and 528 nm, which are attributed to the localized state induced by the presence of oxygen vacancies or defects.^{38,41} The wavelengths of blue emission peaks in this study are longer than the observed wavelengths centered at 405 and 420 nm due to quantum-confinement-effect.^{36,42} The MS sample has another blue emission peak at 414 nm, indicating larger quantity of structural defects, such as oxygen vacancies, on the surface.

Although the BET surface area is similar, the intensity of the blue emission peak of NR-2 is much significantly stronger than those of NR-1. The reason is mainly due to the large exposed (002) polar facets, which contain numerous oxygen vacancies compared to (100) facets. On the other hand, with a similar exposure degree of (002) facets, MS has a considerably higher level of oxygen vacancies and defects than NR-2, which is possibly because of its structural features and large specific surface area. It is believed that the junction between the thin nanorods of each microsphere could increase the density of defects, leading to a stronger intensity of the blue emission peak of the PL spectra in our work. As a surface property, gas sensing of metal oxide semiconductor is significantly related to the density of oxygen vacancies and defects.^{41,43} The highest level of oxygen vacancies and defects on the surface of the MS sample can act as preferential adsorption sites for oxidizing gas

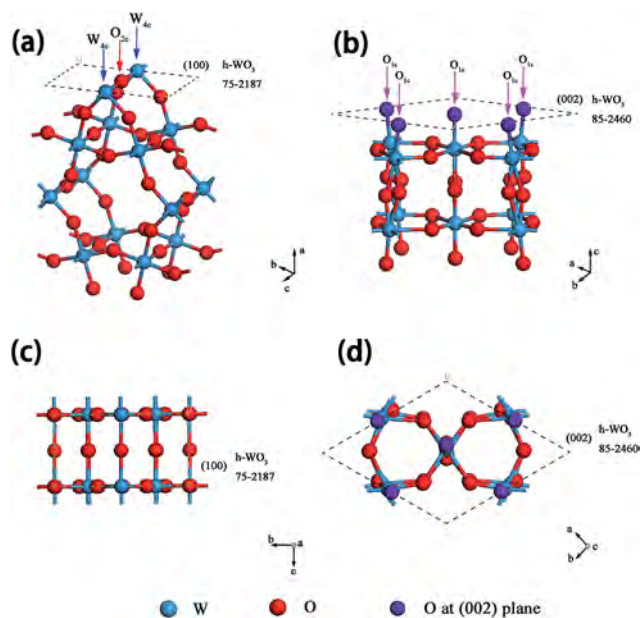


Fig. 9 Geometrical structures of the (100) facet of h- WO_3 from PDF card no. 75-2187 and the (002) facet of h- WO_3 from PDF card no. 85-2460; (a and b) 3D structures, (c and d) top view pictures.

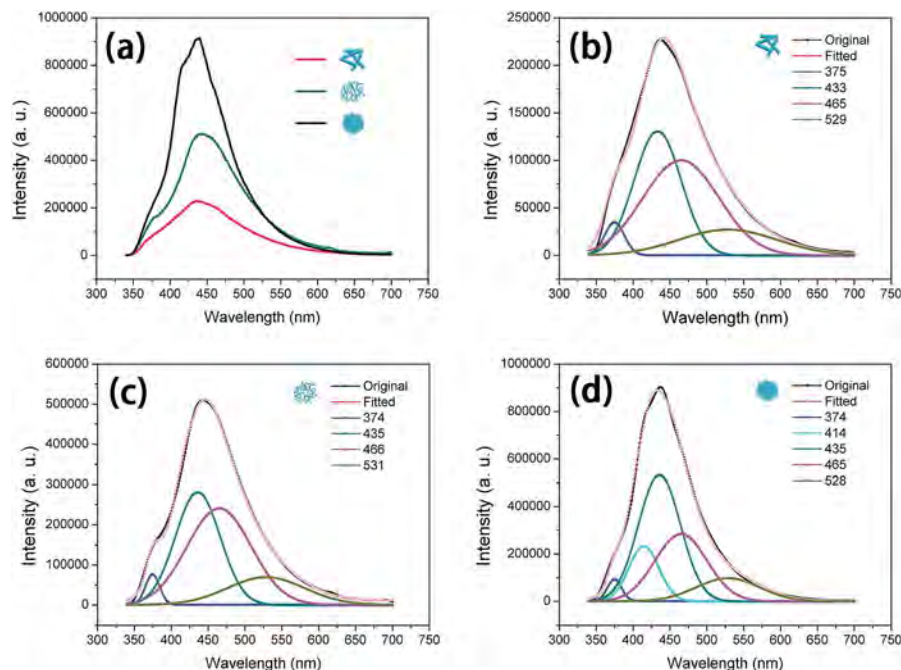


Fig. 10 (a) Room temperature PL spectra of NR-1, NR-2, and MS; and Gaussian fit results of (b) NR-1, (c) NR-2, and (d) MS with the original profiles in black, the Gaussian fit overlaid in red, and the divided peaks in different colors (for interpretation of the references to color in this figure legend, the reader is referred to the web version of this article).

molecules⁴⁴ such that more oxygen species can be absorbed. Once the sample is exposed to acetone, more acetone molecules can react with the absorbed oxygen species. In addition, more structural defects can increase the barrier height of electron mobility, leading to high electric resistance and gas response.

Conclusions

In conclusion, WO₃ nanorods with exposed (100) and (002) facets have been synthesized, and the effect of exposed facets on acetone selective sensing properties are discussed in detail. The (100) facets exposed WO₃ nanorods were sensitive to both acetone and ethanol, while WO₃ nanorods with exposed (002) facets responded selectively to acetone. The microspheres assembled by WO₃ nanorods with (002) facets exhibited a high BET surface area of 62.2 m² g⁻¹, and therefore their response to 1 ppm of acetone was 3.53 with a response and recovery time of 9 and 14 s, respectively, which is the most excellent gas sensitivity reported so far. This selective sensing performance was because the (002) facets comprised unsaturated coordinated O atoms, which were arranged asymmetrically. This asymmetrical distribution caused the distortion of the electron cloud and local electric dipole moment on the surface; thus, it was easier to selectively react with acetone molecules. High gas sensitivity is a result of the large quantity of oxygen vacancies and defects on the (002) facets.

Acknowledgements

The authors are grateful for financial support from the National Natural Science Foundation of China (grant nos. 51172157 and 51202159).

Notes and references

- 1 W. Cao and Y. Duan, *Clin. Chem.*, 2006, **52**, 800–811.
- 2 C. Deng, J. Zhang, X. Yu, W. Zhang and X. Zhang, *J. Chromatogr. B: Anal. Technol. Biomed. Life Sci.*, 2004, **810**, 269–275.
- 3 A. M. Diskin, P. Španěl and D. Smith, *Physiol. Meas.*, 2003, **24**, 107–119.
- 4 V. Khatko, E. Llobet, X. Vilanova, J. Brezmes, J. Hubalek, K. Malysz and X. Correig, *Sens. Actuators, B*, 2005, **111–112**, 45–51.
- 5 A. Hoel, L. F. Reyes, S. Saukko, P. Heszler, V. Lantto and C. G. Granqvist, *Sens. Actuators, B*, 2005, **105**, 283–289.
- 6 J. Kukkola, J. Mäklin, N. Halonen, T. Kyllönen, G. Tóth, M. Szabó, A. Shchukarev, J.-P. Mikkola, H. Jantunen and K. Kordás, *Sens. Actuators, B*, 2011, **153**, 293–300.
- 7 M. Righettoni, A. Tricoli and S. E. Pratsinis, *Anal. Chem.*, 2010, **82**, 3581–3587.
- 8 L. Wang, A. Teleki, S. E. Pratsinis and P. I. Gouma, *Chem. Mater.*, 2008, **20**, 4794–4796.
- 9 S.-J. Choi, I. Lee, B.-H. Jang, D.-Y. Youn, W.-H. Ryu, C. O. Park and I.-D. Kim, *Anal. Chem.*, 2013, **85**, 1792–1796.
- 10 C. Balázs, L. Wang, E. O. Zayim, I. M. Szilágyi, K. Sedlacková, J. Pferfer, A. L. Tóth and P.-I. Gouma, *J. Eur. Ceram. Soc.*, 2008, **28**, 913–917.
- 11 H. Zheng, J. Z. Ou, M. S. Strano, R. B. Kaner, A. Mitchell and K. Kalantar-zadeh, *Adv. Funct. Mater.*, 2011, **21**, 2175–2196.
- 12 L. You, X. He, D. Wang, P. Sun, Y. F. Sun, X. S. Liang, Y. Du and G. Y. Lu, *Sens. Actuators, B*, 2012, **173**, 426–432.
- 13 Z. Liu, M. Miyauchi, T. Yamazaki and Y. Shen, *Sens. Actuators, B*, 2009, **140**, 514–519.

- 14 L. Hu, Q. Peng and Y. Li, *J. Am. Chem. Soc.*, 2008, **130**, 16136–16137.
- 15 X. Han, L. Li and C. Wang, *Chem.–Asian J.*, 2012, **7**, 1572–1575.
- 16 X. Han, M. Jin, S. Xie, Q. Kuang, Z. Jiang, Y. Jiang, Z. Xie and L. Zheng, *Angew. Chem.*, 2009, **121**, 9344–9347.
- 17 R. Boppella, K. Anjaneyulu, P. Basak and S. V. Manorama, *J. Phys. Chem. C*, 2013, **117**, 4597–4605.
- 18 G. R. Li, T. Hu, G. L. Pan, T. Y. Yan, X. P. Gao and H. Y. Zhu, *J. Phys. Chem. C*, 2008, **112**, 11859–11864.
- 19 M. R. Alenezi, A. S. Alshammari, K. D. G. I. Jayawardena, M. J. Beliatas, S. J. Henley and S. R. P. Silva, *J. Phys. Chem. C*, 2013, **117**, 17850–17858.
- 20 S. Tian, F. Yang, D. Zeng and C. Xie, *J. Phys. Chem. C*, 2012, **116**, 10586–10591.
- 21 J. Zhu, S. Wang, S. Xie and H. Li, *Chem. Commun.*, 2011, **47**, 4403–4405.
- 22 H. Zhang, M. Yao, L. Bai, W. Xiang, H. Jin, J. Li and F. Yuan, *CrystEngComm*, 2013, **15**, 1432–1438.
- 23 A. Gurlo, *Nanoscale*, 2011, **3**, 154–165.
- 24 L. Saadi, C. Lambert-Mauriat, V. Oison, H. Ouali and R. Hayn, *Appl. Surf. Sci.*, 2014, **293**, 76–79.
- 25 L. Zhao, F. H. Tian, X. Wang, W. Zhao, A. Fu, Y. Shen, S. Chen and S. Yu, *Comput. Mater. Sci.*, 2013, **79**, 691–697.
- 26 X. Bai, H. Ji, P. Gao, Y. Zhang and X. Sun, *Sens. Actuators, B*, 2014, **193**, 100–106.
- 27 H. Z. Zhang, X. C. Sun, R. M. Wang and D. P. Yu, *J. Cryst. Growth*, 2004, **269**, 464–471.
- 28 A. Phuruangrat, D. J. Ham, S. J. Hong, S. Thongtem and J. S. Lee, *J. Mater. Chem.*, 2010, **20**, 1683–1690.
- 29 K. S. W. Sing, D. H. Everett, R. A. W. Haul, L. Moscou, R. A. Pierotti, J. Rouquérol and T. Siemieniowska, *Pure Appl. Chem.*, 1985, **57**, 603–619.
- 30 N. D. Hoa and S. A. El-Safty, *Anal. Methods*, 2011, **3**, 1948–1956.
- 31 Z. Gu, T. Zhai, B. Gao, X. Sheng, Y. Wang, H. Fu, Y. Ma and J. Yao, *J. Phys. Chem. B*, 2006, **110**, 23829–23836.
- 32 J. Shin, S.-J. Choi, D.-Y. Youn and I.-D. Kim, *J. Electroceram.*, 2012, **29**, 106–116.
- 33 P. Gao, H. Ji, Y. Zhou and X. Li, *Thin Solid Films*, 2012, **520**, 3100–3106.
- 34 H. Meixner and U. Lampe, *Sens. Actuators, B*, 1996, **33**, 198–202.
- 35 J. A. Dean, *Lange's Handbook of Chemistry*, 1985.
- 36 C.-Y. Su and H.-C. Lin, *J. Phys. Chem. C*, 2009, **113**, 4042–4046.
- 37 Y.-H. Li, Y. M. Zhao, R. Z. Ma, Y. Q. Zhu, N. Fisher, Y. Z. Jin and X. P. Zhang, *J. Phys. Chem. B*, 2006, **110**, 18191–18195.
- 38 K. Lee, W. S. Seo and J. T. Park, *J. Am. Chem. Soc.*, 2003, **125**, 3408–3409.
- 39 M. Feng, A. L. Pan, H. R. Zhang, Z. A. Li, F. Liu, H. W. Liu, D. X. Shi, B. S. Zou and H. J. Gao, *Appl. Phys. Lett.*, 2005, **86**, 141901.
- 40 Y. M. Zhao, W. B. Hu, Y. D. Xia, E. F. Smith, Y. Q. Zhu, C. W. Dunnill and D. H. Gregory, *J. Mater. Chem.*, 2007, **17**, 4436–4440.
- 41 P. V. Tong, N. D. Hoa, V. V. Quang, N. V. Duy and N. V. Hieu, *Sens. Actuators, B*, 2013, **183**, 372–380.
- 42 S. Sun, X. Chang and Z. Li, *Mater. Res. Bull.*, 2010, **45**, 1075–1079.
- 43 L. Liao, H. B. Lu, J. C. Li, H. He, D. F. Wang, D. J. Fu, C. Liu and W. F. Zhang, *J. Phys. Chem. C*, 2007, **111**, 1900–1903.
- 44 M.-W. Ahn, K.-S. Park, J.-H. Heo, J.-G. Park, D.-W. Kim, K. J. Choi, J.-H. Lee and S.-H. Hong, *Appl. Phys. Lett.*, 2008, **93**, 263103.